Journal of Nuclear Materials 406 (2010) 138–151

Contents lists available at ScienceDirect

Journal of Nuclear Materials

journal homepage: www.elsevier.com/locate/jnucmat

Localized deformation as a key precursor to initiation of intergranular stress corrosion cracking of austenitic stainless steels employed in nuclear power plants

Wade Karlsen [a,*], Gonzalo Diego [b], Bastian Devrient [c]

[a] VTT Technical Research Centre of Finland, P.O. Box 1000, FI-2044 VTT, Finland
[b] CIEMAT, Technology Department, Material Division. Avda. Complutense, 22, 28040 Madrid, Spain
[c] AREVA NP GmbH Materials Technology, Materials Laboratories – NTCMM-GFreyeslebenstraße 1, 91058 Erlangen, Germany

A B S T R A C T

Cold-work has been associated with the occurrence of intergranular cracking of stainless steels employed in light water reactors. This study examined the deformation behavior of AISI 304, AISI 347 and a higher stacking fault energy model alloy subjected to bulk cold-work and (for 347) surface deformation. Deformation microstructures of the materials were examined and correlated with their particular mechanical response under different conditions of temperature, strain rate and degree of prior cold-work. Select slow-strain rate tensile tests in autoclaves enabled the role of local strain heterogeneity in crack initiation in pressurized water reactor environments to be considered. The high stacking fault energy material exhibited uniform strain hardening, even at sub-zero temperatures, while the commercial stainless steels showed significant heterogeneity in their strain response. Surface treatments introduced local cold-work, which had a clear effect on the surface roughness and hardness, and on near-surface residual stress profiles. Autoclave tests led to transgranular surface cracking for a circumferentially ground surface, and intergranular crack initiation for a polished surface.

© 2010 Elsevier B.V. All rights reserved.

1. Introduction

Austenitic stainless steels are widely used in light water reactor components due to their good combination of elevated temperature mechanical performance and corrosion resistance. Nonetheless, stress corrosion cracking (SCC) has occurred in some particular components simultaneously exposed to mechanical load and a light water reactor (LWR) environment. Important to the continued safe operation of power plants is assurance of the integrity of the materials of their construction, so there is a need for a better understanding of the factors that can contribute to such cracking. Intergranular stress corrosion cracking (IGSCC) is characterized by crack propagation along the material's grain boundaries. While factors such as chromium depletion at grain boundaries (sensitization) and oxidizing environments have been shown to be important contributing factors to IGSCC incidences [1], cracking has also occurred in non-sensitized stainless steels exposed to low-potential pressurized water reactor (PWR) primary and secondary environments [2]. More recently the role of cold-work in promoting IGSCC has gained more broad attention [3]. Power plants utilize materials which have been intentionally cold-worked in order to achieve better mechanical performance, but cold-working of a material can also occur during fabrication, in conjunction with shrinkage at welds and e.g. at regions that have undergone grinding.

Cold-work is important because it is intimately linked to the material's mechanical behavior. Cold-work typically leads to an increase in yield strength and a decrease in ductility in austenitic stainless steels. However, two other important parameters also affect the mechanical behavior of a given austenitic stainless steel: the test (operation) temperature and the rate of material straining. An increase in test temperature leads to a decrease in the yield strength and uniform elongation, while a slower strain rate typically enables a higher maximum stress to be reached [4,5]. Both of these effects are related to the strain hardening behavior of austenitic stainless steels.

The underlying reasons for the observed strain hardening behavior lie in the deformation mechanisms and deformation kinetics operating in the material. The deformation mechanisms possible within the face-centered cubic (fcc) lattice of austenitic materials are particularly diverse, but they all tend to occur the most readily at the close-packed cube-diagonal of the lattice (i.e. on the {1 1 1} planes). In austenitic stainless steels in particular, close competition exists between classical dislocation motion, and the displacive transformation of a finite volume of material via mechanical twinning or martensite phase formation.

Underpinning the competition between the mechanisms is the stacking fault energy (SFE) of the material. Equivalent strain

* Corresponding author. Tel.: +358 20 722 6865; fax: +358 20 722 7002.
E-mail address: wade.karlsen@vtt.fi (W. Karlsen).

0022-3115/$ - see front matter © 2010 Elsevier B.V. All rights reserved.
doi:10.1016/j.jnucmat.2010.01.029

transmission can occur with less energy expenditure by the zig-zagging of two partial dislocations whose Burgers vectors sum to the Burgers vector of the strain increment. Separation of a pair of partial dislocations produces an extended dislocation containing a stacking fault between the partial dislocations. Because the SFE of a material is inversely proportional to the equilibrium distance between those two separated partial dislocations, a lower SFE allows broad separation of the partial dislocations. Broadly-separated partial dislocations impede multi-plane cross-slip, relegating slip to certain planes (planar slip) and thereby accelerating the entanglement of dislocations. At a basic level the SFE of a material is mostly a function of its chemistry. The aforementioned diversity of deformation mechanisms in austenitic stainless steels is largely a consequence of the fact that the SFE of austenitic stainless steels is generally considered to be "low" or "medium", with a partial dislocation separation distance of about 10 nm without external stress [6]. Several numerical values for the actual SFE of the different austenitic stainless steels can be found in the literature, but in general 304L stainless steel is deemed to have a slightly lower SFE than 316L, about 17–26 mJ m^{-2} vs. 25–64 mJ m^{-2}, respectively [7,8].

Several displacive transformations can also occur in deformed austenitic stainless steels. At sufficiently high stresses, deformation twinning can shear the austenite matrix parallel to the close-packed {1 1 1} plane in the ⟨1 1 2⟩ direction. Likewise, the accumulation of stacking faults on every other austenite close-packed plane can ultimately result in the formation of epsilon martensite, having a hexagonal close packed (hcp) structure. Particularly important is also the formation of body-centered cubic (bcc) alpha-prime martensite phase, which has been researched extensively on account of the magnetic properties it imparts to otherwise non-magnetic austenitic stainless steels. Because the displacive transformations occur in finite volumes within the lattice, they effectively interrupt the dislocation glide path, and so contribute to the hardening of the material [5,9,10].

The particular deformation temperature is important because it dictates the most energy-economical means of transmitting the required strain, and thereby the predominant deformation mechanism. Low temperatures typically promote displacive transformation, while higher temperatures favor dislocation processes. Byun et al. found that 316LN stainless steel deformed at sub-zero temperatures exhibited twins, stacking faults and/or martensite laths along with dislocations, whereas dislocation-dominant microstructures were exhibited following elevated temperature deformation [9]. Likewise, Botshekan et al. specifically looked at the effect of temperature on strain-induced alpha-prime martensite evolution in 316LN, as measured by the magnetic-at-saturation method, finding that no alpha-prime martensite was formed upon deformation to rupture at room temperature, but there was a clear increase in alpha-prime martensite content with increasing strain in both tensile and low-cycle fatigue tests at −198 °C [11]. On the other hand, dislocation motion is a thermally activated process, so increasing temperatures clearly promote slip over displacive deformation processes. Increasing the temperature also increase the vacancy content and diffusion rates of vacancies, so vacancy-accelerated dislocation climb and glide are more prominent with increasing temperature. Likewise, dislocation movement leads to dynamic recovery in the material by the annihilation of dislocations of opposite sign. That has the effect of reducing the number of dislocations left to interact with obstacles and one another, which counteracts strain hardening [5].

In the same manner as increasing temperature enhances the kinetics of dislocation-related deformation mechanisms, for a given mechanism, a slower strain rate gives more time for its manifestation. For that reason the rate of loading a material can have a significant effect on the consequent mode of strain transmission, and/or on the stress at which straining occurs. That is regularly observed in tensile tests conducted at moderate and low strain rates (10^{-5}–10^{-8}/s), in which strain transmission by dislocations occurs more readily and with more uniform sustainability with reduced strain rates (i.e. the flow stress is reduced). On the other hand, straining at more rapid rates (e.g. >10/s) tends to promote displacive deformations like twinning [12].

Of particular interest to crack initiation, is the heterogeneity of deformation within a material. The most obvious case of heterogenous deformation is the onset of necking in a tensile test, when the strain localizes on a macro level when the maximum engineering stress is reached. However, as a consequence of processes such as post-weld material shrinkage or surface machining or grinding, local cold-work can alter the local material condition. This can lead to non-uniform deformation response on a more local scale. On a still finer scale, heterogeneous deformation can also occur in a multi-grained material due to the randomness of the lattice orientation with respect to the critical resolved shear stress. Utilizing single-crystal 316L, Karaman et al. showed that different deformation mechanisms predominated at different orientations of shear stress with respect to the crystal lattice, and consequently different strain hardening rates were achieved [13]. As some grains are more suitably oriented for deformation, they undergo more deformation in particular directions than their neighboring grains, resulting in a heterogeneous distribution of local strain. Strain may also be localized within a single grain, as a consequence of the formation of shear bands due to some of the slip planes being more active than their adjacent ones, often due to the presence of obstacles such as inclusions or precipitates. This is particularly prevalent in irradiated materials, which undergo so-called channel deformation when strain is localized to bands cleared of small irradiation-induced obstacles [14]. In the case of intergranular cracking, the effect of such strain localization impinging on grain boundaries is of interest [15].

This article describes cooperative work carried out within the framework of the EU project PERFECT, focused on characterizing the deformation behavior of austenitic stainless steels employed in nuclear power plants, and extension of that to the case of strain response heterogeneity due to surface cold-work, for a discussion of its implications for IGSCC crack initiation in light water reactor (LWR) environments.

2. Experimental

The materials used in the study included two commercial austenitic stainless steels, one being non-stabilized AISI 304 and the other being niobium-stabilized AISI 347 (GMN 1.4550), as well as a higher SFE model alloy. The compositions of the materials are shown in Table 1, along with the SFE as calculated from Pickering's equation [16]

$$\mathrm{SFE}\ (\mathrm{mJ\,m^{-2}}) = 25.7 + 2\ (\%\mathrm{Ni}) + 410\ (\%\mathrm{C}) - 0.9\ (\%\mathrm{Cr}) - 77\ (\%\mathrm{N}) - 13\ (\%\mathrm{Si}) - 1.2\ (\%\mathrm{Mn})$$

Basic characterization of the mechanical behavior of the materials was done by carrying out tensile tests at several different temperatures, strain rates, and levels of prior cold-work, as summarized in Table 2. Cold-work was carried out in three different manners: cold-drawing via die drawing was used for some of the 304 material, pre-straining in a tensile test machine at room temperature was used for the model alloy and the rest of the 304 material, while cross-rolling of slabs cut from thick round-bar stock was utilized for the 347 material. Tensile specimens were of two types: thin plate or round bar. The thin plate specimens had a nominal thickness of 2 mm and a gauge width and length of 2.5 and 10 mm, respectively. For the drawn rod, round bar specimens were

Table 1
Composition of alloys of this study and their calculated stacking fault energy.

Material	Alloying wt.%-balance Fe									SFE (mJ m^{-2})
	C	Cr	Ni	Si	Mn	P	S	Mo	Nb	
304	0.04	18.4	8.5	0.33	1.56	0.033	0.020	–	–	36
347	0.026	18.5	10.7	0.18	1.83	0.021	0.001	0.3	0.5	36
Model	0.026	11.9	27.9	2.63	0.96	0.018	0.004	0.38	–	45

Table 2
The mechanical test matrix carried out in this study.

Material	Bar morphology	Condition	CW%	Temp.	Strain rate
304	Round	Cold-drawn	30	300 °C	3.0×10^{-4}
304	Round	Cold-drawn	30	300 °C	1.0×10^{-5}
304	Round	Cold-drawn	30	Room	3.0×10^{-4}
304	Thin plate	Mill annealed	–	Room	1.0×10^{-4}
304	Thin plate	Mill annealed	–	Room	$1.0 \times 10^{+0}$
304	Thin plate	Tensile CW	30	Room	1.0×10^{-4}
304	Thin plate	Tensile CW	30	Room	$1.0 \times 10^{+0}$
304	Thin plate	Mill annealed	–	−75 °C	1.0×10^{-4}
304	Thin plate	Mill annealed	–	−75 °C	$1.0 \times 10^{+0}$
304	Thin plate	Tensile CW	30	−75 °C	1.0×10^{-4}
304	Thin plate	Tensile CW	30	−75 °C	$1.0 \times 10^{+0}$
304	Thin plate	Mill annealed	–	−150 °C	1.0×10^{-4}
304	Thin plate	Mill annealed	–	−150 °C	$1.0 \times 10^{+0}$
304	Thin plate	Tensile CW	30	−150 °C	1.0×10^{-4}
304	Thin plate	Tensile CW	30	−150 °C	$1.0 \times 10^{+0}$
347	Thick plate	Mill annealed	–	Room	5.0×10^{-4}
347	Thick plate	Cross-rolled	10	Room	5.0×10^{-4}
347	Thick plate	Cross-rolled	20	Room	5.0×10^{-4}
347	Thick plate	Cross-rolled	30	Room	5.0×10^{-4}
347	Thick plate	Cross-rolled	40	Room	5.0×10^{-4}
347	Thick plate	Cross-rolled	50	Room	5.0×10^{-4}
347	Thick plate	Mill annealed	–	290 °C	5.0×10^{-4}
347	Thick plate	Cross-rolled	10	290 °C	5.0×10^{-4}
347	Thick plate	Cross-rolled	20	290 °C	5.0×10^{-4}
347	Thick plate	Cross-rolled	30	290 °C	5.0×10^{-4}
347	Thick plate	Cross-rolled	40	290 °C	5.0×10^{-4}
347	Thick plate	Cross-rolled	50	290 °C	5.0×10^{-4}
Model alloy	Thin plate	Mill annealed	–	Room	1.0×10^{-4}
Model alloy	Thin plate	Mill annealed	–	Room	$1.0 \times 10^{+0}$
Model alloy	Thin plate	Mill annealed	–	−50 °C	1.0×10^{-4}
Model alloy	Thin plate	Mill annealed	–	−50 °C	$1.0 \times 10^{+0}$
Model alloy	Thin plate	Mill annealed	–	−100 °C	1.0×10^{-4}
Model alloy	Thin plate	Mill annealed	–	−100 °C	$1.0 \times 10^{+0}$
Model alloy	Thin plate	Mill annealed	–	−150 °C	1.0×10^{-4}
Model alloy	Thin plate	Mill annealed	–	−150 °C	$1.0 \times 10^{+0}$

used with a gauge diameter of 3 mm and a length of 10 mm, while for the 347 material round bars had a gauge diameter of 6 mm and length of 30 mm.

In order to examine the effect of conditions closer those present in LWR applications, a series of additional tests were carried out in slow-strain rate tensile (SSRT) test autoclaves, as summarized in Table 3. While most of the tests were carried out with round bars having a 3 mm diameter gauge region 10 mm long, the gauge region of VTT6 was ground and polished flat. Electron beam lithography was then used to apply a fine grid of thin, gold lines on the flat surface in order to measure the extent of strain heterogeneity in the material. The surfaces of VTT3, VTT4 and VTT7 had been left in the as-ground condition, while the rest were polished with 5 μm diamond paste. The PWR primary environment was 1200 ppm B, 2.1 ppm Li and had 30 cc/kg H_2. At 300 °C it was 120 bar and at 340 °C it was 160 bar.

To examine the effect of surface work, the AISI 347 material in each of the cold-work conditions was subjected to four different levels of mechanical material removal. The basis surface finish was represented by longitudinal grinding by a corundum disk, producing a finish corresponding to that comparable to most technical surfaces in a power plant. An improved surface was produced by further polishing with SiC paper followed by 3 μm diamond paste. On the other hand, atypical surfaces were produced by either grinding with an angle grinder with an abrasive cut-off wheel of grit size 80 (called Flex80), or by using a milling machine to produce a series of discrete, longitudinal gouges in the surface with a cone-shaped spike. The roughness of the resultant surfaces was then characterized by measuring the profiles in the transverse and longitudinal directions with a standard contact profilometer device. The microhardness at the surface for each condition was also measured. The residual stress in the near-surface region was measured by X-ray analysis for the 0% and 50% cold-work conditions. A residual stress profile was obtained from the surface into the bulk of the 50% cold-work material by electrochemically removing layers of material, repeating the residual stress measurements at each layer.

The manifestation of deformation at the surface of the specimens was examined by scanning electron microscopy (SEM). The deformation microstructure of the materials was characterized by transmission electron microscopy (TEM). For examinations of the bulk deformation behavior, several 3 mm diameter specimens were prepared for each material condition of interest, first thinning by standard mechanical grinding, and then thinning to electron-transparency by electrolytic polishing. The microstructure in the deformed layer adjacent to the surface of the surface-treated AISI 347 material was examined in foils prepared at a depth of approximately 50–200 μm.

3. Results

3.1. Tensile behavior

The tensile properties of the tested materials are shown in Table 4. Several observations can be made regarding the measured tensile properties. Firstly, it is evident that at room temperature and moderate strain rate in the annealed condition, the model alloy had lower yield strength (YS) than either the 304 or the 347, while the 304 reached a much higher ultimate tensile strength (UTS) and elongation than the other two materials. While the 347 reached a higher YS and UTS than the model alloy, it had slightly less elongation before fracture. For the 30% cold-worked condition, the drawn

Table 3
Autoclave tests carried out on 30% cold-drawn 304 stainless steel in this study.

ID	Load type	Bar and surface	Temp. (°C)	Condition[a]	Plastic strain at test end (%)	Environment
VTT6	SSRT	Flat, grid, polished round	300	7×10^{-8}	6.5	PWR
VTT7	SSRT	Ground round	340	7×10^{-8}	6.5	PWR
VTT8	SSRT	Polished round	300	7×10^{-8}	6.5	PWR + Li
VTT9	SSRT	Polished	300	7×10^{-8}	6.5	Argon

[a] Constant strain test began at an initial stress of 553 MPa, while constant load test was maintained at 553 MPa for the duration of the test.

AISI 304 and cross-rolled AISI 347 had comparable YS and UTS at both room temperature and elevated temperature, but the elongation of the former was about double that of the latter at both temperatures. In both of those materials the elevated temperature properties were inferior to the room temperature properties though. As expected, cold-working of the AISI 347 material led to higher YS and UTS, but lower elongation to fracture. On the other hand, while pre-straining the 304 in a tensile machine to 30% cold-work significantly increased its room temperature YS with only a small reduction in the elongation, the YS achieved was still lower than that of the 304 cold-worked to the same level by drawing. Predictably, the drawn 304 material tested at elevated temperature at a slower strain rate yielded at a slightly lower stress level, but achieved a higher UTS and elongation to fracture than the one tested at the standard strain rate. Likewise, the 304 thin plate materials in both annealed and 30% tensile pre-strain yielded at a higher stress but achieved lower UTS and elongation to fracture when the strain rate was significantly higher than the standard rate, and that was true not only for room temperature tests, but also held for most of the tests at sub-zero temperatures as well. A similar response was observed for the high SFE model alloy, except that at the higher strain rate the material reached a *higher* UTS than at the standard strain rate. Finally, with decreasing sub-zero test temperature, all of the properties of the model alloy increased at both strain rates, but for the 304 material, only the UTS increased consistently for both strain rates and for both annealed and cold-worked condition. The YS of the 304 material was highest at −75 °C for both strain rates and conditions, while its fracture elongation seemed to decrease with decreasing temperature.

3.2. Strain hardening behavior

The properties displayed by the materials under the different conditions are largely a function of the strain hardening behavior of the materials. Selected tensile curves for the materials are shown in Figs. 1–6. Several aspects of the behavior are noteworthy. Firstly, it is immediately evident that the particular material, its condition and test conditions resulted in a broad variety of behaviors. For the 347 material, strain localization/plastic instability set in at an early stage, with the *extent* of localization more pronounced with increasing level of prior cold-work, particularly in the tests conducted at boiling water reactor (BWR) temperature, but also in the tests conducted at room temperature. By contrast, at room temperature the 304 material in annealed, 30% pre-strained and 30% cold-drawn conditions, and at both high and moderate strain rate, all showed some degree of strain hardening over most of the plastic region, with plastic instability setting in

Table 4
Tensile properties measured for the materials of this study under the various conditions.

Material	Temp. (°C)	Strain rate (s^{-1})	Cold-work (%)	YS (MPa)	UTS (MPa)	Elong. (%)
304 drawn	300	1.0×10^{-5}	30	590	679	30
304 drawn	300	3.0×10^{-4}	30	605	656	21
304 drawn	RT	3.0×10^{-4}	30	710	845	50
304 thin plate	RT	1.0×10^{-4}	0	349	651	108
304 thin plate	RT	$1.0 \times 10^{+0}$	0	360	663	80
304 thin plate	−75	1.0×10^{-4}	0	367	1058	80
304 thin plate	−75	$1.0 \times 10^{+0}$	0	485	917	75
304 thin plate	−150	1.0×10^{-4}	0	352	1296	79
304 thin plate	−150	$1.0 \times 10^{+0}$	0	429	1087	67
304 pre-strained	RT	1.0×10^{-4}	30	517	641	82
304 pre-strained	RT	$1.0 \times 10^{+0}$	30	575	634	59
304 pre-strained	−75	1.0×10^{-4}	30	570	937	72
304 pre-strained	−75	$1.0 \times 10^{+0}$	30	635	801	67
304 pre-strained	−150	1.0×10^{-4}	30	537	1143	73
304 pre-strained	−150	$1.0 \times 10^{+0}$	30	625	960	63
Alloy 347	290	5.0×10^{-4}	0	150	386	44
Alloy 347	290	5.0×10^{-4}	10	435	465	19
Alloy 347	290	5.0×10^{-4}	20	593	637	13
Alloy 347	290	5.0×10^{-4}	30	630	672	10.5
Alloy 347	290	5.0×10^{-4}	40	675	772	10.5
Alloy 347	290	5.0×10^{-4}	50	742	863	9.5
Alloy 347	RT	5.0×10^{-4}	0	295	585	60
Alloy 347	RT	5.0×10^{-4}	10	553	660	45.7
Alloy 347	RT	5.0×10^{-4}	20	699	766	27.5
Alloy 347	RT	5.0×10^{-4}	30	739	832	24
Alloy 347	RT	5.0×10^{-4}	40	762	923	19
Alloy 347	RT	5.0×10^{-4}	50	911	1064	14
Model alloy	RT	1.0×10^{-4}	0	180	420	70
Model alloy	RT	$1.0 \times 10^{+0}$	0	287	583	51
Model alloy	−50	1.0×10^{-4}	0	273	553	83.5
Model alloy	−50	$1.0 \times 10^{+0}$	0	296	682	51
Model alloy	−100	1.0×10^{-4}	0	290	595	91.5
Model alloy	−100	$1.0 \times 10^{+0}$	0	381	768	59.3
Model alloy	−150	1.0×10^{-4}	0	314	677	96
Model alloy	−150	$1.0 \times 10^{+0}$	0	452	740	59

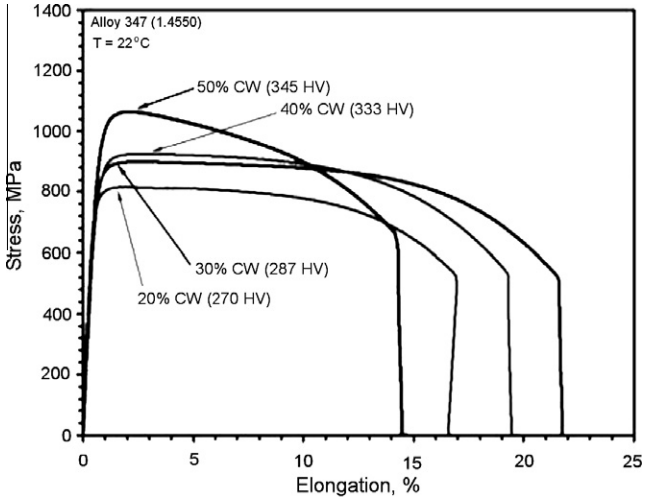

Fig. 1. Tensile engineering stress–elongation behavior of cross-rolled AISI 347 at room temperature, for several levels of cold-work.

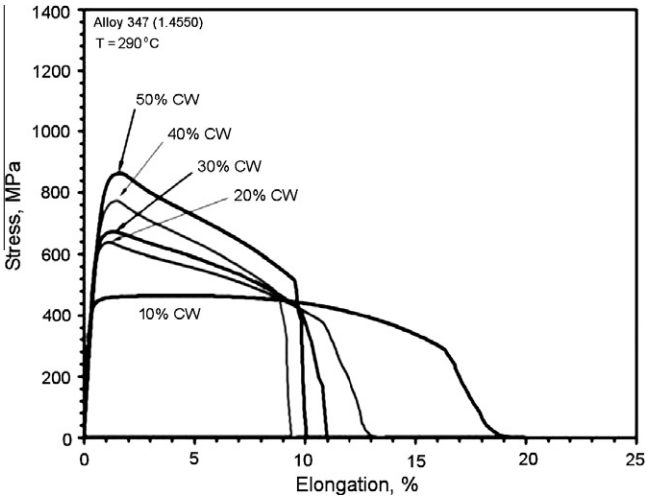

Fig. 2. Tensile engineering stress–elongation behavior of cross-rolled AISI 347 at 290 °C, for several levels of cold-work.

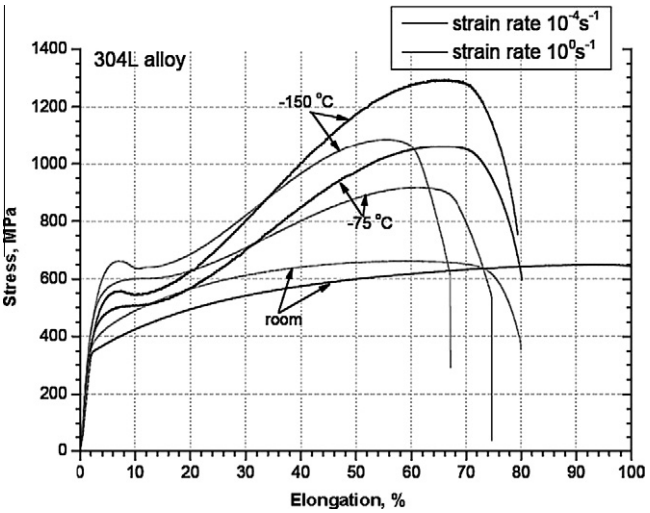

Fig. 3. Tensile engineering stress–elongation behavior of the AISI 304 in the annealed condition, for several temperatures and two strain rates.

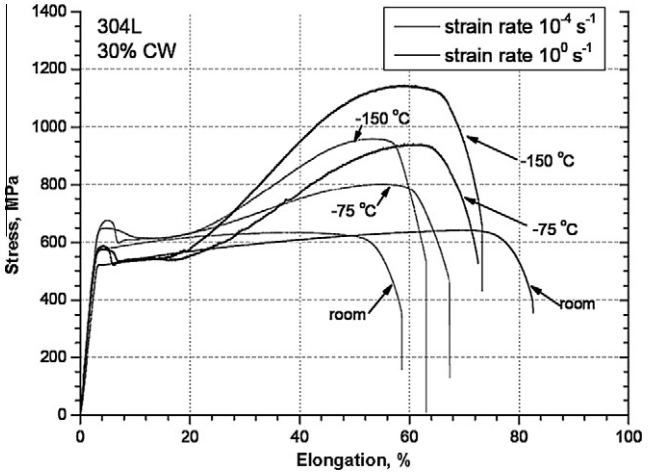

Fig. 4. Tensile engineering stress–elongation behavior of the AISI 304 in the 30% pre-strained condition, for several temperatures and two strain rates.

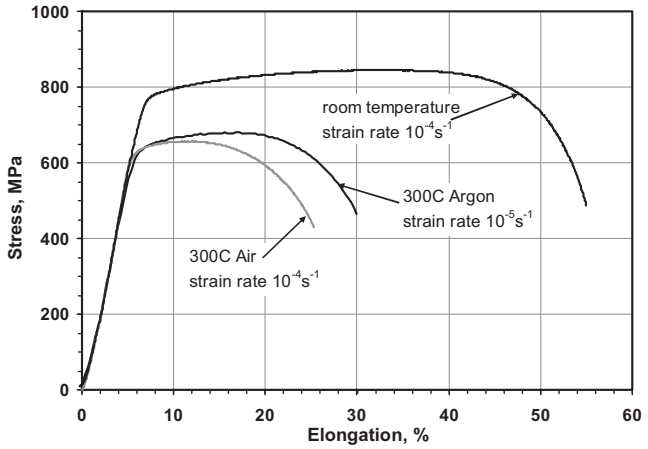

Fig. 5. Tensile engineering stress–elongation behavior of the AISI 304 in the 30% cold-drawn condition, at room temperature and at two strain rates at elevated temperature.

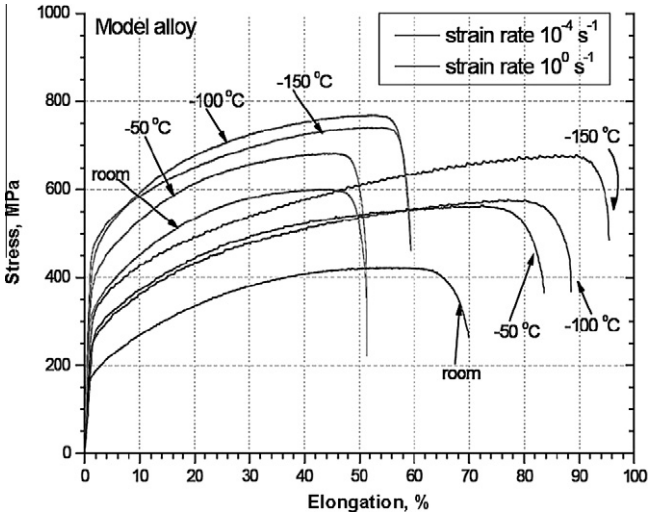

Fig. 6. Tensile engineering stress–elongation behavior of the model alloy in the annealed condition, for several temperatures and two strain rates.

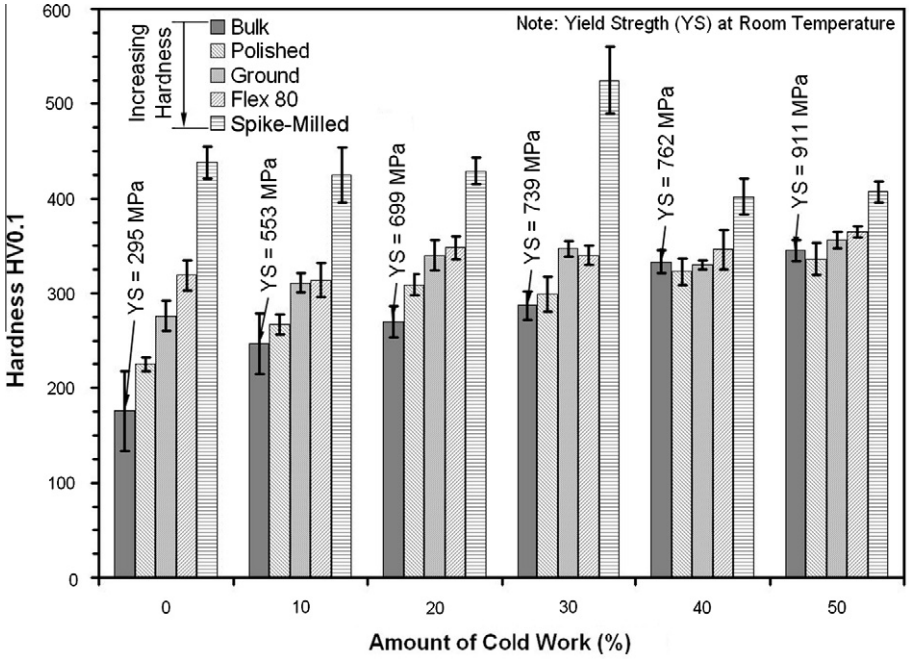

Fig. 7. Surface hardness resulting from each surface treatment at each cold-work level (expressed as percent reduction).

Table 5
Surface roughness resulting from the different surface mechanical treatments.

Condition	R_a μm		R_Z μm		R_{max} μm	
	Long.	Trans.	Long.	Trans.	Long.	Trans.
Polished	0.05 ± 0.0	0.06 ± 0.0	0.3 ± 0.0	0.3 ± 0.0	0.3 ± 0.0	0.9 ± 0.0
Ground	0.40 ± 0.02	0.49 ± 0.19	2.4 ± 0.21	2.5 ± 0.17	4.8 ± 0.32	4.9 ± 0.55
Flex80	0.95 ± 0.17	1.07 ± 0.20	7.7 ± 0.86	6.4 ± 1.6	8.2 ± 1.0	8.1 ± 1.3
Spike–milled	0.12 ± 0.19	0.72 ± 0.34	0.8 ± 1.5	6.3 ± 1.8	0.9 ± 3.1	10.0 ± 4.6

Note: The values from the roughness measurements are mean values from three different profiles. Three profiles in "Long" and "Trans" direction respectively. The direction of spike milling was in "Long" direction, thus the R_z and R_{max} value have high scatter.

only after significant uniform elongation. However, in the tests conducted at sub-zero temperatures the extent of strain hardening in the 304 material was not only remarkable, but occurred in a complex manner. At early stages a short period of strain softening or strain localization occurred, which was then followed by a stage of rapid hardening, and then finally a reduction in the rate of hardening as the maximum stress was reached and plastic instability set in. The behavior was similar at all sub-zero test temperatures and for both strain rates. On the other hand, the high stacking fault energy model alloy tested in the same conditions showed uniform strain hardening behavior to a moderate maximum stress before plastic instability set in.

Table 6
Results of residual stress measurements via X-ray diffraction on flat bars following the different surface mechanical treatments.

Cold-work (%)	Surface condition	Axial stress (MPa)	Tangent. stress (MPa)
0	Polished	−259 ± 91	−464 ± 118
	Ground	−170 ± 105	−565 ± 71
	Flex80	−293 ± 38	+215 ± 34
	Spike-milled	+304 ± 90	−228 ± 47
50	Polished	−299 ± 15	−422 ± 13
	Ground	−232 ± 10	−520 ± 18
	Flex80	−133 ± 24	+110 ± 25
	Spike-milled	+12 ± 82	−45 ± 120

3.3. Surface treatment effects

Moving to the results of surface finishes, Fig. 7 shows the measured surface hardness values for each cold-work condition following each surface treatment, together with the bulk hardness for each cold-work level. Each method increased the surface hardness over the bulk, but the spike-milled treatment clearly had the greatest affect. However, as the bulk hardness increased due to bulk cold-work, the difference between surface and interior decreased, such that at 40% and 50% cold-work it was virtually the same for all but the spike-milled surface. Table 5 shows the roughness values in the transverse and longitudinal directions resulting from each surface method when the material was in the annealed condition. Clearly the roughness increased from the polished to the spike-milled surface. The spike-milled surface had a high standard deviation due to its nature consisting of a series of discrete grooves. The residual stresses are shown in Table 6 for the 0% and 50% cold-work conditions. It is evident that the polishing and grinding methods both produced compressive stresses in the surface, but the Flex80 method resulted in significant tensile tangential stresses and the spike-mill method resulted in significant tensile axial stresses. In the 50% cold-worked condition those stresses were less than in the non-cold-worked condition though, and in both conditions the residual stresses were compressive in the other direction.

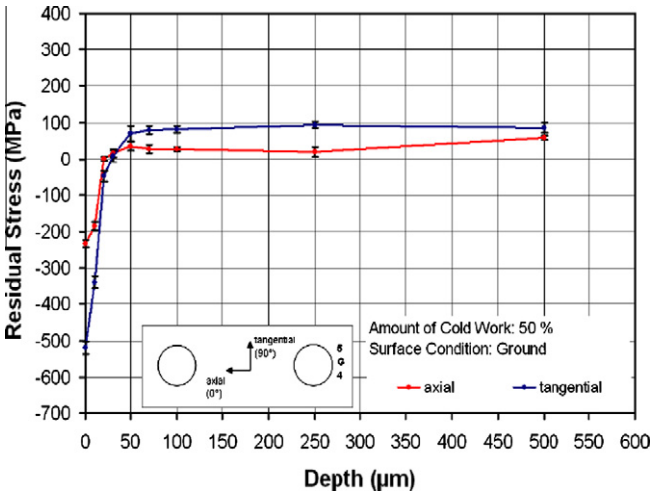

Fig. 8. Residual stress profile of 50% cold-worked 347 in the "Ground" surface condition.

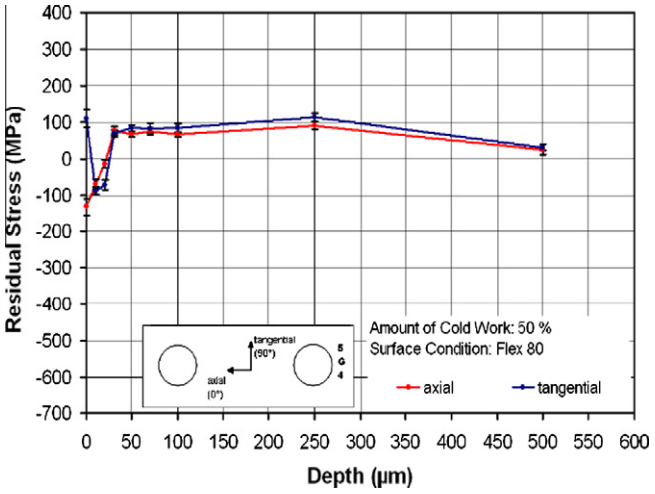

Fig. 9. Residual stress profile of 50% cold-worked 347 in the "Flex80" surface condition.

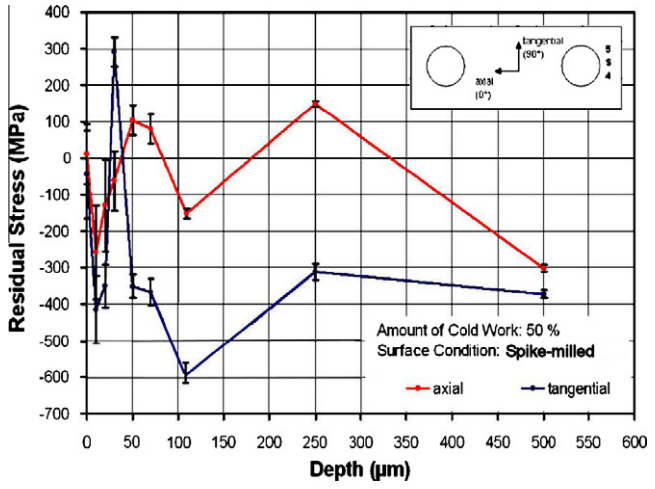

Fig. 10. Residual stress profile of 50% cold-worked 347 in the "spike-milled" surface condition.

Table 7
Quantification of crack density.

Specimen	Image mag.	Line length (mm)	No. of cracks	Cracks (mm)	Mode
VTT6-PWR	100×	1.19	76	64	IG
VTT6-PWR	250×	0.34	26	77	IG
VTT7-HiT PWR	100×	1.19	107	90	TG
VTT7-HiT PWR	250×	0.34	54	160	TG
VTT8-PWR + Li	100×	1.19	28	24	IG
VTT8-PWR + Li	250×	0.34	12	36	IG
VTT9-argon	100×	1.19	0	0	None
VTT9-argon	250×	0.34	0	0	None

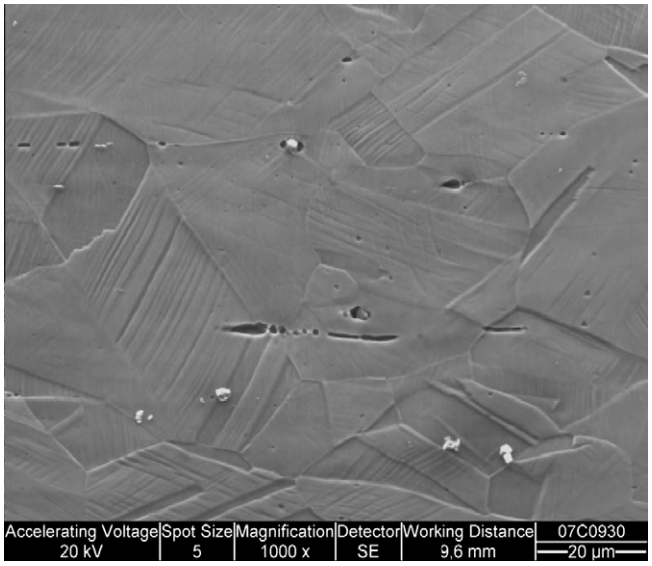

Fig. 11. SEM examination of the surface of the SSRT bar tested at 300 °C in argon revealed a clean surface and no cracks. The elongated features are stringers aligned axially with the test bar, e.g. with the tensile test direction.

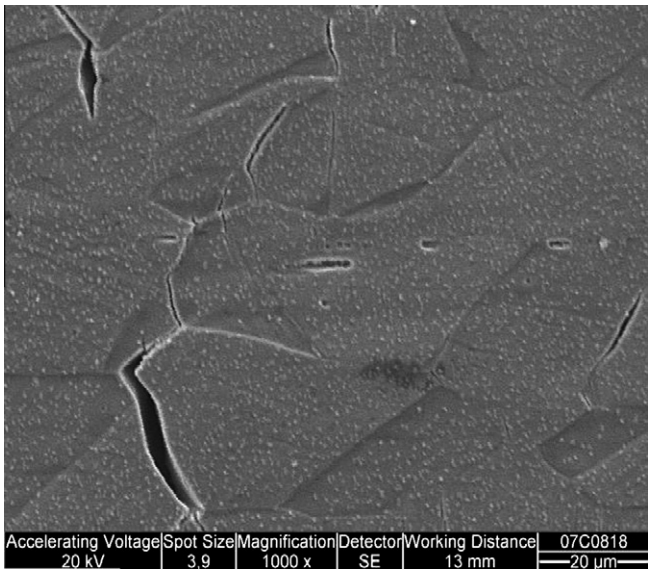

Fig. 12. SEM examination of the surface of the SSRT bar VTT6, tested in 300 °C PWR environment, showed some oxide crystals on surface, yet slip-steps were still visible in many grains. IG cracking was also clearly present, perpendicular to the tensile direction.

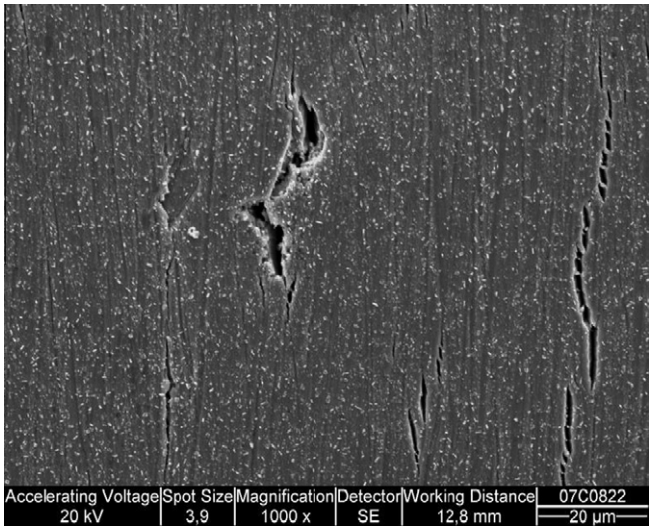

Fig. 13. SEM examination of the surface of the SSRT bar VTT7, tested in 340 °C PWR environment, showed that TG cracks were present perpendicular to tensile axis. The cracks were clearly associated with the fine grooves in the surface. Since the surface was not polished prior to testing, slip-steps were not visible.

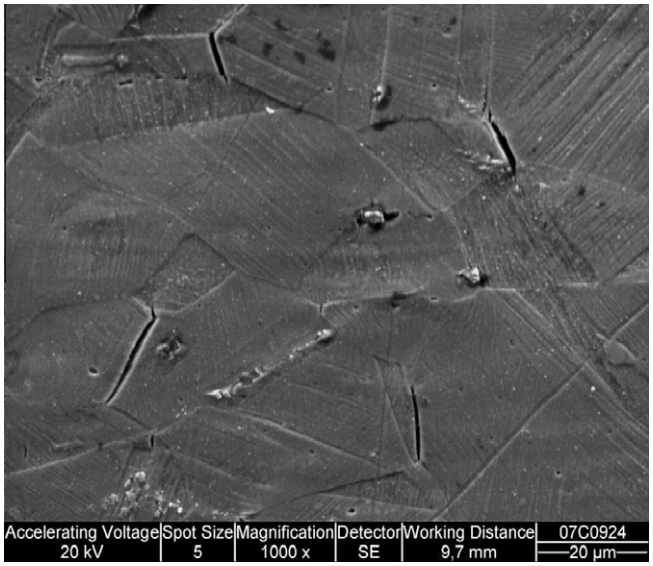

Fig. 14. SEM examination of the surface of the SSRT bar VTT8, tested in 300 °C PWR environment with elevated Li content, showed that IG cracks were present perpendicular to tensile axis, while slip-steps are also visible. The surface also appears to be cleaner than that of VTT6.

Finally, the residual stress profiles measured for the three most aggressive surface methods for the 50% cold-worked condition are shown in Figs. 8–10. While both Ground and Flex80 conditions produced fairly uniform axial stress profiles, going from compressive at the surface to tensile in the interior, the spike-mill method produced very heterogeneous residual stresses that varied dramatically with orientation and depth between tensile and compressive.

3.4. Crack initiation tests

The specimen surface condition is of particular interest with respect to the case of crack initiation in an environment, as was examined in the interrupted SSRT tests of this study. The number of cracks for each interrupted SSRT sample was calculated using a line-intercept method on the SEM images for each material, the

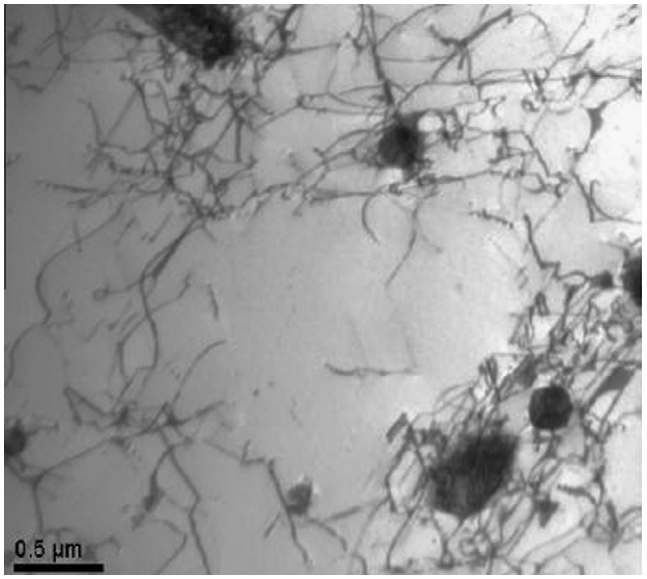

Fig. 15. In the 347, the density of dislocations was generally higher in the vicinity of the niobium carbides, as shown here for the annealed condition.

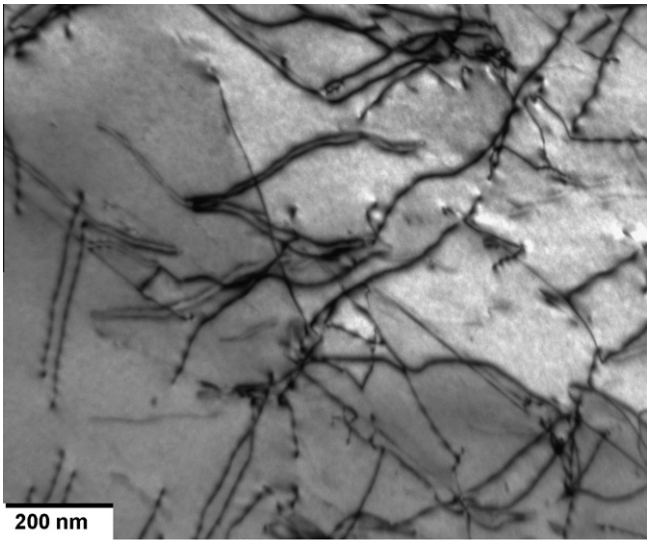

Fig. 16. The deformed high SFE model alloy mostly showed perfect dislocations, as in this image from material deformed at room temperature and strain rate of 10^{-4} s^{-1}.

results of which are shown in Table 7. As shown in Fig. 11, the bar tested in argon (VTT9) showed no cracking. There was, however, a significant population of slip-steps visible at the polished surface. The surface itself was quite clean, with an obvious absence of oxide crystallites that one could expect following cooling from a PWR primary environment. The elongated features are inclusion stringers aligned with the test-bar axis, so also correspond to the tensile test direction in the material. In Fig. 12 it can be seen that the surface of the SSRT bar VTT6, tested in a 300 °C PWR primary environment, showed clear IG cracking perpendicular to the tensile direction. Some oxide crystals were present on the surface as well, though slip-steps were still visible in many grains. On the other hand, as shown in Fig. 13, the SSRT bar tested in 340 °C PWR environment showed TG cracks perpendicular to the tensile axis. The cracks were clearly associated with the fine grooves in the surface. SEM examination of the surface of the SSRT bar VTT8, tested in 300 °C PWR environment with elevated Li content, showed that

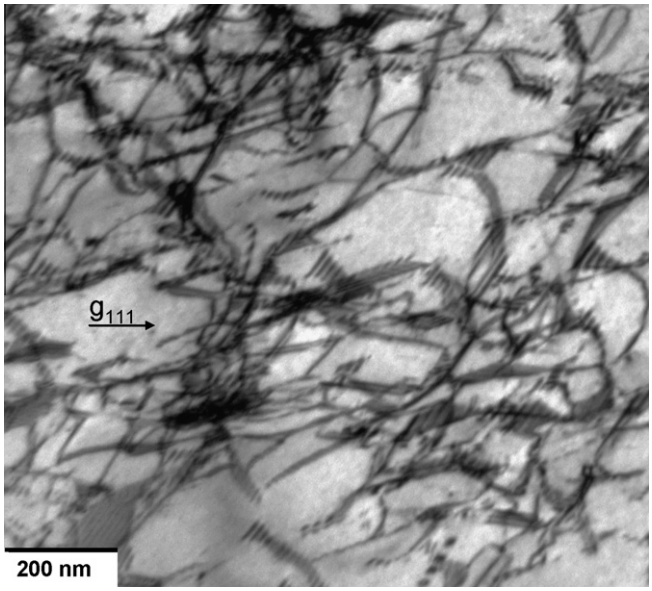

Fig. 17. The deformation of the annealed 304 stainless steel produced partial dislocations with stacking faults, as in this image from material deformed at room temperature and strain rate of 10^{-4} s^{-1}.

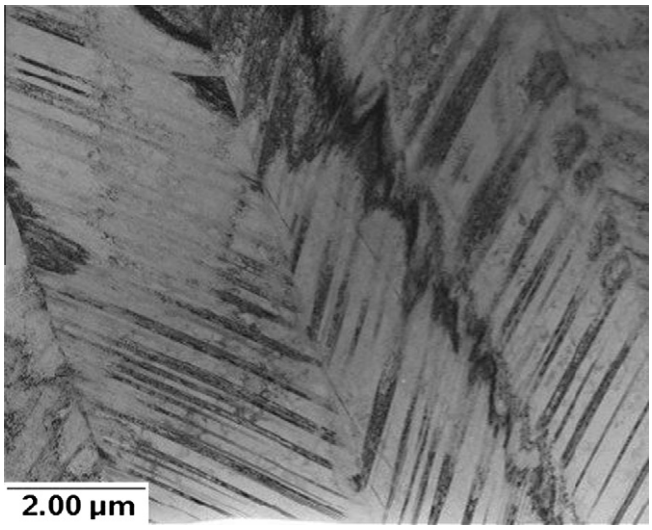

Fig. 18. In the 30% cold-drawn condition, the 304 material showed significant banding in the deformation microstructure.

IG cracks were present perpendicular to tensile axis, and that slip-steps are also visible, Fig. 14. The surface also appeared to be cleaner than that of VTT6.

3.5. Results of transmission electron microscopy

TEM examinations were carried out on the materials in a range of conditions. In general, all three materials in the annealed condition showed a low density of dislocations, with the density of dislocations increasing with increasing amount of cold-work. In the 347, the density of dislocations was generally higher in the vicinity of the niobium carbides, as shown in Fig. 15. While in the high SFE model alloy the deformation microstructure consisted mostly of perfect dislocations (Fig. 16), the stainless steels all showed signs of stacking fault formation in addition to the perfect dislocations (Fig. 17). Subsequent cold-working of the stainless steels led to distinct bands in both the 304 and 347 materials, as shown in Figs. 18 and 19, respectively. Such planar slip bands were often associated with hcp martensite formation (Fig. 20). The population of such bands increased with increasing level of cold-work, strain rate and strain accumulation, and with lower temperature, an example of which is shown in Fig. 21 for the annealed 304 tested at −150 °C and a strain rate of 10^0 s^{-1}. The 304 stainless steel in both cold-drawn and tensile pre-strained conditions also showed evidence of twinning (Fig. 22), and at the intersections of epsilon martensite bands, the formation of alpha martensite was detected (Fig. 23). As shown in Fig. 24, the bulk alpha martensite content of the 347 increased rapidly with increased level of cold-work, so correlates well with the TEM observations made on the 304 material. When the slip bands intersected a grain boundary, significant blooms of high dislocation density were often evident in the adjacent grain, suggesting a lack of strain transmission to the primary slip planes of the neighbor grain (Fig. 25). Of particular interest, however, is the near-surface microstructure of the annealed 347 exposed to different kinds of surface mechanical treatments. As shown in the collage of Fig. 26, the microstructure showed clear evidence of cold-work associated with the different methods, with the dislocation density increasing in the order polished → ground → Flex80 → spike-milled.

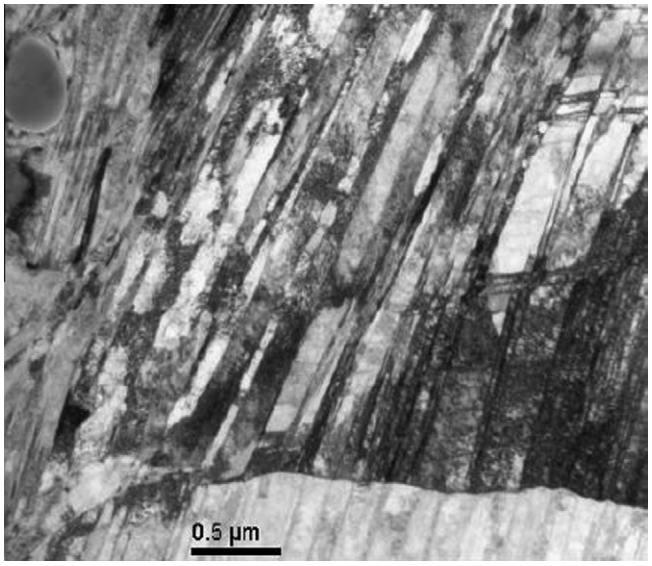

Fig. 19. With increasing amount of cross-rolling, the extent of planarity within the deformation microstructure of the 347 increased, as shown here for the 40% cold-worked condition.

4. Discussion

The principle goal of this study was to examine the deformation behavior of three different austenitic stainless steels, and then apply that understanding to the case of surface mechanical treatment for a discussion of the role that local strain heterogeneity may play in crack initiation. The mechanical tests demonstrated how the particular microstructure, SFE and level of cold-work of the three stainless steels produced different mechanical performance and strain hardening behavior as a function of the particular test temperature and strain rate. Underlying the mechanical performance was the deformation behavior in the different cases, as manifested in the microstructures observed. The importance of SFE was demonstrated by the fact that the model alloy did not show a significant population of stacking faults or planarization of slip, but rather, the dislocations remained as perfect or very closely spaced

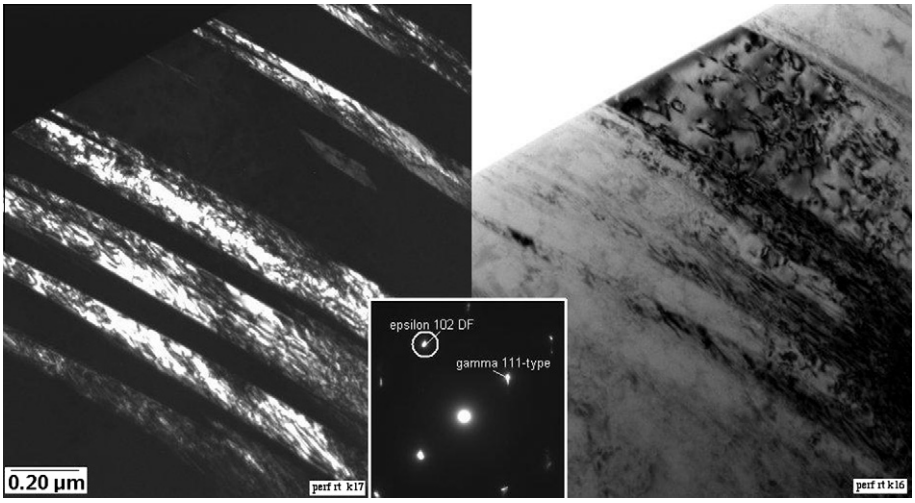

Fig. 20. Further straining at room temperature led to bands of epsilon martensite, shown here for the 30% cold-drawn 304.

pairs of partial dislocations. Because in this configuration the dislocations are more free to cross-slip, they have much greater freedom of motion, which was manifested as uniform strain hardening not only at room temperature, but also at faster strain rates and at lower temperatures, where the driving force for dislocation motion is higher but energy availability is lower. On the other hand, in the lower stacking fault energy 304 material, the separation of the dislocations into pairs of partial dislocations was much more pronounced. The stacking fault formed between them restricts cross-slip, which promoted strain localization to the principle slip planes, manifested as parallel slip bands visible in the microstructure. That in turn encouraged strain hardening, which was evident in that fact that, while at room temperature in the annealed condition the 304 and model alloy showed similar strain hardening behavior, at higher strain rates and lower temperatures the 304 showed much greater extent of strain hardening than the high SFE model alloy.

Cold-work prior to tensile testing encouraged the evolution of the planar deformation structure in the lower SFE materials, but further straining at room temperature also led to both epsilon and martensite phase formation. Twinning was also observed, most likely as a consequence of strain hardening enabling the critical twinning stress to be reached. In 347 the fraction of alpha-prime martensite was shown to increase as a function of cold-work. Thus, in addition to the planar slip, the phase transformations could also be expected to contribute to the significant increase in strength observed as a consequence of cold-work and straining at lower temperatures, particularly in the case of the 304 materials tested at sub-zero temperatures, where the energy availability for dislocation motion was much lower.

The initial yield drop exhibited by the 304 material at the sub-zero temperatures may be a symptom of strain localization, in that with such a high driving force yet low energy availability, yielding may have initially occurred only on the few most favorable planes, which would produce the distinct deformation bands that were observed in the deformed microstructure in those test materials. Particularly in the case of the faster strain rate, adiabatic heating may also be partially responsible for the initial softening observed. The concept of adiabatic heating is discussed in more detail by Talonen [5], but its effect is to locally raise the temperature in the material, thereby enhancing dislocation glide, and thus straining.

Meanwhile, the presence of the population of niobium carbides in the 347 material was most likely responsible for the fact that, for comparable material conditions and test temperatures, the 347 material consistently exhibited more significant localized plasticity and overall lower elongation to fracture than did the 304 material. Because the niobium carbides pose a hard obstacle to dislocation motion, they contribute to the basic strength of the material, but they significantly shorten the mean free path of the gliding dislocations. Since the interface between the niobium carbide particle and the matrix offers a ready site for the micro-decohesion preceding fracture, that reduces the extent of elongation attainable before fracture initiates.

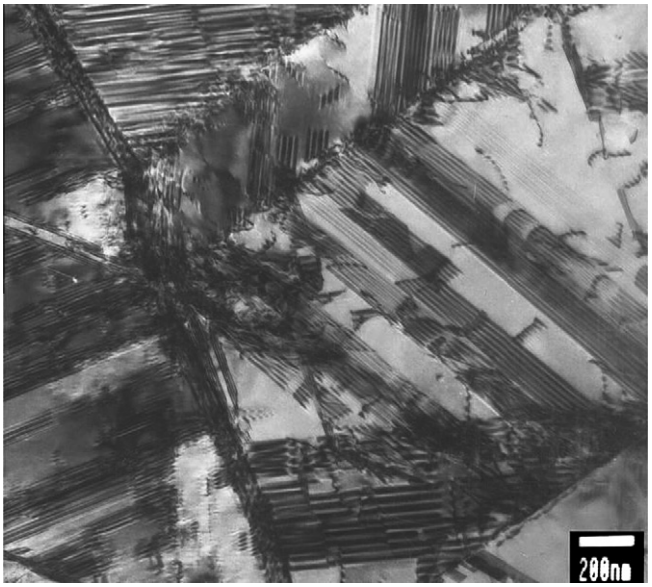

Fig. 21. With lower temperature and higher strain rate the planarization was even more pronounced, as shown here for the annealed 304 tested at −150 °C and a strain rate of 1 s^{-1}.

The aforementioned aspects of the deformation behavior of the material would also be true for the case of the surface mechanical work. The increase in hardness accompanying the surface treatments can be directly correlated with the appearance of their corresponding deformation microstructures. The correlation is similar to that between the bulk hardness and cold-work microstructures. The cold-work suffered by the material as a consequence of the work put into the surface by the pressure of the abrading media would seem to be commensurate with the relative size and load

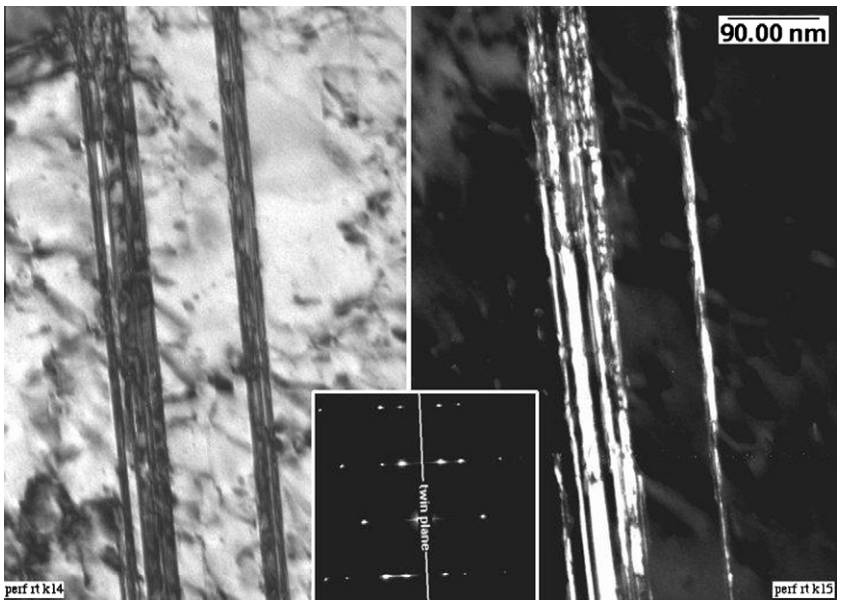

Fig. 22. Further straining at room temperature also led to deformation twinning, shown here for the 30% cold-drawn 304.

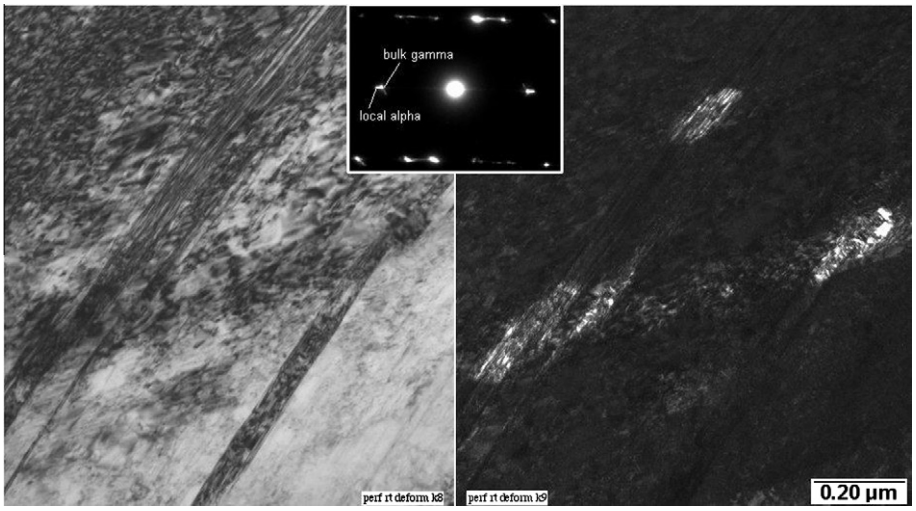

Fig. 23. Further straining of the 30% cold-drawn 304 at room temperature also led to the nucleation of alpha martensite at the intersection of epsilon martensite bands.

involved in the particular process, with the Flex80 producing the equivalent of 40% cold-work. That was also reflected in the residual stresses at the surface, in which the more significantly cold-worked surfaces exhibited less favorable residual stress profiles, and in particular the spike-milled surface had a dramatic variance that would seem to correlate well with the deformation one could expect from a single point load gouging the surface. Of most significance though, is that stress corrosion crack initiation has typically been associated with a local hardness exceeding 300 HV [17]. Referring back to Fig. 7, it is apparent that only 40% or more cold-work led to that hardness being exceeded in the bulk. However, once surface mechanical treatment was superimposed on the bulk condition, both the Flex80 and spike-milled surfaces exceeded that hardness level in all cases, while grinding raised the hardness over that threshold in the 10% cold-worked condition, and even polishing left an unsatisfactory hardness level at the surface of the 20% cold-worked material.

Finally, considering the above results in conjunction with the 30% cold-drawn 304 SSRT test results brings the discussion even closer to

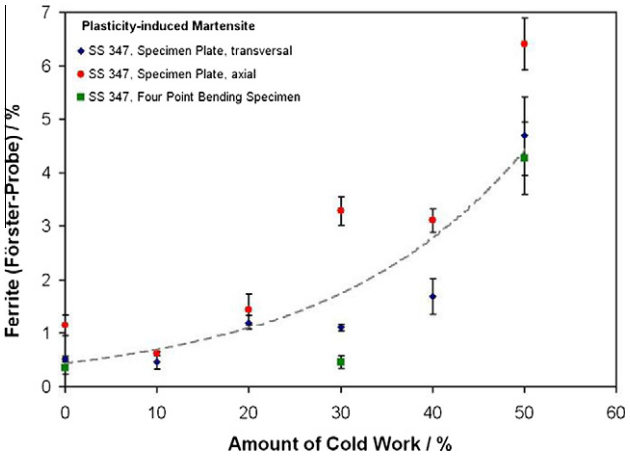

Fig. 24. Alpha martensite content in 347 as a function of the level of cold-work.

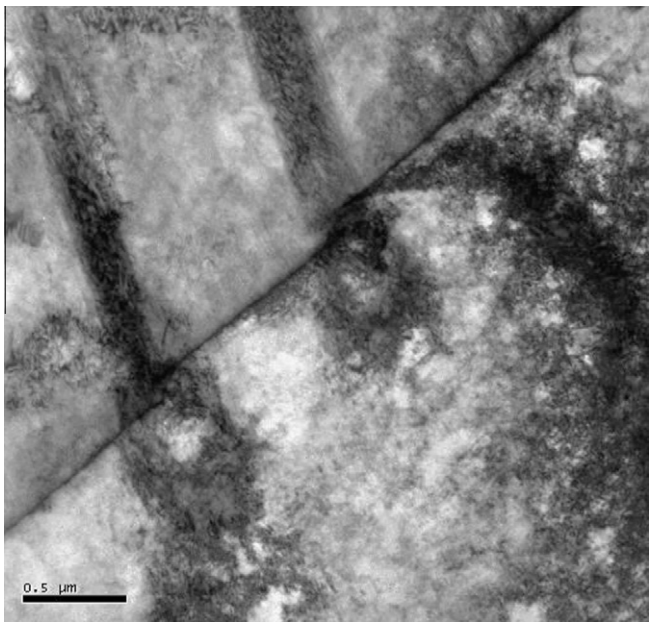

Fig. 25. When the slip bands intersected a grain boundary, significant blooms of high dislocation density were often evident in the adjacent grain, as shown here for the 30% tensile pre-strained 304 subsequently tested at −150 °C and strain rate of $1\ s^{-1}$. The scale is 0.5 μm.

the case of crack initiation in power plant components. Revisiting the results shown in Table 7, it is apparent that cracking was most significant in the higher temperature PWR water test showing transgranular cracks, but cracks also initiated in the two other SSRT tests conducted in a PWR environment, and in an intergranular manner. Meanwhile, no cracking had yet occurred at the equivalent macro strain level in the bar tested in argon environment. In the higher temperature test in PWR water the test bar had a ground surface, and the cracks clearly initiated in the valleys of the grinding marks. Thus, two kinds of factors were likely: the temperature and the surface condition. The preceding discussion has demonstrated that the surface grinding could be expected to produce additional cold-work at the surface, while the cold-drawing process itself also set up a pre-existing population of slip bands in the matrix. The results of the relaxation test also demonstrated that at the elevated temperatures some recovery can be expected, which could locally plasticize the material. Thus, it is conceivable that the cold-worked surface could relax at the PWR temperature, enabling straining to progress locally, and thereby lead to crack initiation.

On the other hand, in the polished material the cracking occurred intergranularly. The difference is most likely due to the additional effect of the notch formed by the root of the circumferential scratches in the ground case, which would be sufficient to concentrate the stresses in those regions in that case. The principle processes operating are still most likely the strain localization in the strongly banded structure of the cold-drawn material.

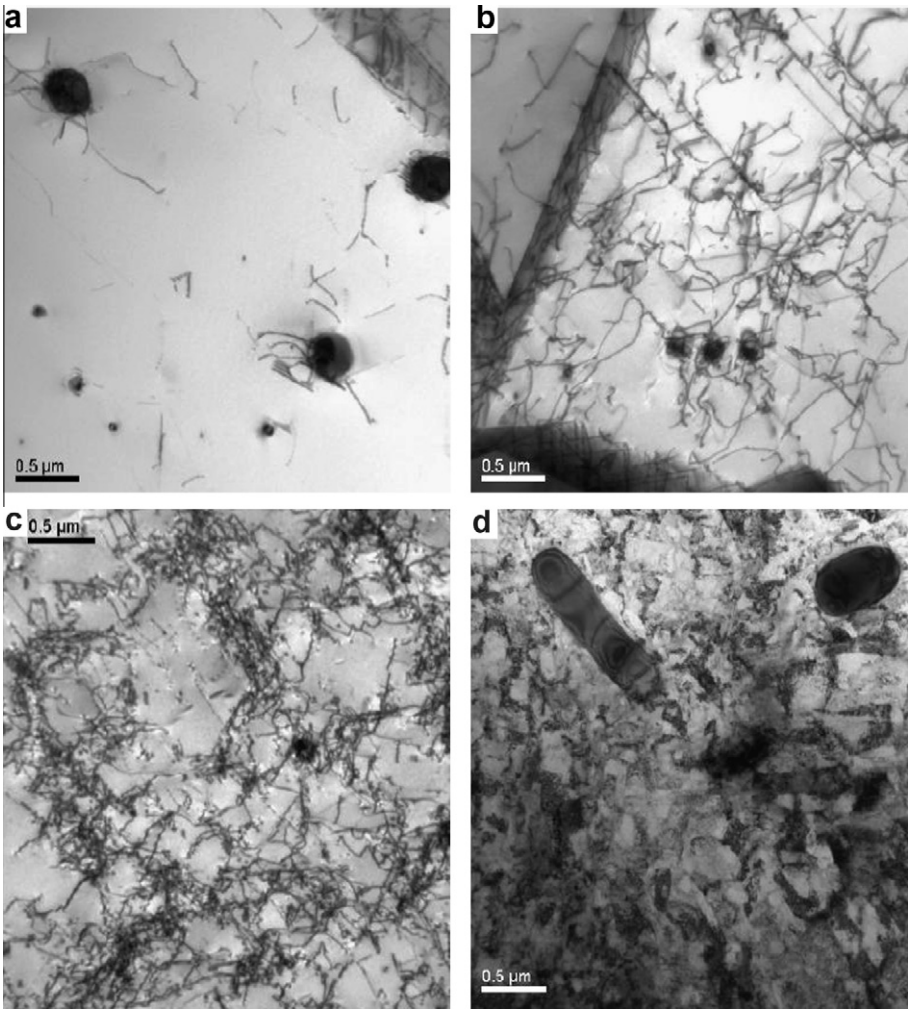

Fig. 26. The extent of cold-work induced in the annealed 347 surface by the different mechanical treatments is evident in the deformation microstructures of each case: (a) polished, (b) ground, (c) Flex80 and (d) spike-milled. The scale is 0.5 μm in each image.

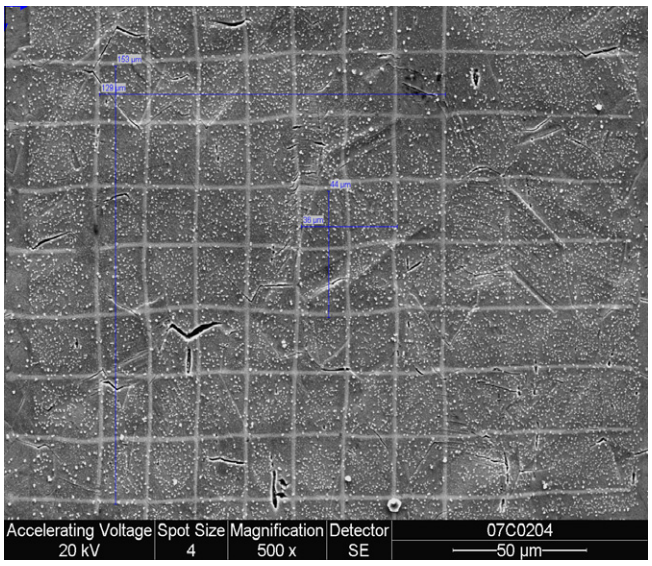

Fig. 27. The gold grid produced by electron beam lithography on the flat gauge region of the VTT6 remained intact following autoclave testing. The distortion of the grid lines demonstrates the non-uniform deformation resulting from variations in critical resolved shear stress between adjacent grains.

When the slip bands terminate at a grain boundary and the neighboring grain's orientation thwarts effective strain transmission, an increase in the local stress can be expected. Likewise, when an aggregate of grains of random orientation are considered, there is the additional level of heterogeneity imposed by the difference in local critical resolved shear stress for the particular strain bands orientation. As was described earlier, a gold grid was utilized on the VTT6 specimen. As shown in Fig. 27, what was originally a symmetrical square grid became elongated in the direction of the applied load during the SSRT test. More importantly though, is that individual lines were distorted along with the underlying test material, demonstrating the non-uniform manifestation of strain resulting from the aforementioned variations in the critical resolved shear stress between adjacent grains. Lin Peng et al. studied the development of residual intergranular strains in 3 mm thick 304 stainless steel sheets strained to 0.2%, 7.5%, 29.8%, and 44.7% peak plastic strain [18]. Neutron diffraction measurements were used to quantify the lattice planar spacing (d-spacing) upon straining and then unloading. Comparing those measured values to the original d-spacing provided a direct indication of the intergranular plastic strains incurred. They found that intergranular strains increased with the level of plastic strain incurred in the test bar as a whole, with the magnitude and sign of "strain" within each grain being a function of the particular grain's orientation. The combination of strain heterogeneity both at the grain aggregate level, and via slip band within the grains, would most likely enhance the local residual stresses. In the case of residual stresses already pre-existing due to a more aggressive surface mechanical treatment like the Flex80 or spike-milled surfaces of this study, the effect could be even greater. Thus, the residual stresses arising locally from such pre-straining scenarios in the materials of real components could be expected to be an important precursor to crack initiation. In fact, SEM examinations of the surfaces of the 40% and 50% cold-worked 347 material following tensile testing at 290 °C found some cases of apparent grain boundary sliding in conjunction with crack initiation, as shown in Fig. 28.

Finally, the fact that cracks had not yet initiated at the 6.5% strain level in the argon environment when they *had* initiated in the PWR environments, points out the additional role played by the environment. In the presence of an aqueous environment there is the possibility for corrosion processes to take place. From a deformation standpoint, of particular interest is the possibility that corrosion processes at the material surface can result in the injection of additional vacancies into the material locally [19,20]. Various researchers have considered a role for corrosion-produced vacancies in interacting with dislocations, enhancing dislocation mobility to produce increased creep rates locally [21–23]. Thus, in this case it seems likely that such corrosion-enhanced plasticity acting in conjunction with the localized planar slip was responsible for cracks initiation in the PWR environments when they did not initiate in the argon environment in this study.

5. Conclusions

The principle goal of this study was to examine the deformation behavior of three different austenitic stainless steels, and then apply that understanding to the case of surface mechanical treatment, for a discussion of the role that local strain heterogeneity may play in crack initiation in LWR components. The work lead to the following conclusions:

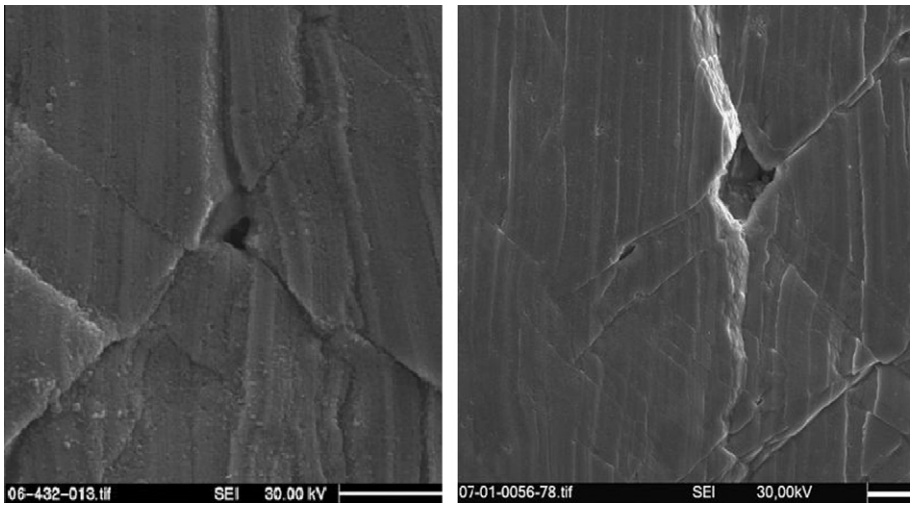

Fig. 28. SEM micrographs from the exterior of deformed round bar specimens of 40% (left) and 50% cold-worked 347 following tensile testing at 290 °C, showing indications of grain boundary sliding preceding fracture.

- The high SFE material exhibited uniform strain hardening even at sub-zero temperature, and exhibited deformation microstructures consisting primarily of networks of perfect dislocations.
- The lower SFE commercial stainless steels showed significant heterogeneity in their strain response, sensitive to both temperature and strain rate, as well as to the degree of prior cold-work. The complex response was correlated with deformation microstructures exhibiting planar slip and deformation products such at epsilon and alpha martensite as well as micro twins, all features which accelerate the rate of strain hardening, but also promote strain localization at a granular scale.
- The surface treatments on the 347 material affected the surface roughness of the materials and introduced local cold-work, which had a clear effect on the surface hardness and near-surface residual stress profiles. The deformation microstructures correlated well with equivalent levels of bulk cold-work.
- SSRT tests of 30% cold-worked 304 in PWR environment initiated copious transgranular cracks with a ground surface condition and intergranular cracks with a polished surface.
- Strain heterogeneity promotes strain localization, which in turn promotes crack initiation.

Acknowledgment

The authors thank the European project PERFECT for financial support (Contract Number: F160-CT-2003-508840).

References

[1] P.L. Andresen, K. Gott, J.L. Nelson, in: Proceedings of Ninth International Symposium on Environmental Degradation of Materials in Nuclear Power Systems – Water Reactors, AIME, 1999.
[2] P.L. Andresen, T.M. Angeliu, L.M. Young, W.R. Catlin, R.M. Horn, Mechanisms and Kinetics of SCC in Stainless Steels, in: Proceedings of Tenth International Symposium on Environmental Degradation of Materials in Nuclear Power Systems – Water Reactors, NACE, 2001.
[3] P.L. Andresen, T.M. Angeliu, W.R. Catlin, L.M. Young, R.M. Horn, Corrosion/2000, Paper 00203, NACE, 2000.
[4] A.M. Cuitiñio, Mater. Sci. Eng. A216 (1996) 104–116.
[5] J. Talonen, Effect of strain-induced α'-martensite transformation on mechanical properties of metastable austenitic stainless steels, Ph.D. Thesis, Helsinki University of Technology, 2007, <http://lib.tkk.fi/Diss/2007/isbn9789512287802>.
[6] T.S. Byun, Acta Mater. 51 (2003) 3063–3071.
[7] S. Catalao, X. Feaugas, Ph. Pilvin, M.-Th. Cabrillat, Mater. Sci. Eng. A 400–401 (2005) 349–352.
[8] B. Ravi Kumar, B. Mahato, N.R. Bandyopadhyay, D.K. Bhattacharya, Mater. Sci. Eng. A 394 (2005) 296–301.
[9] T.S. Byun, N. Hashimoto, K. Farrell, Acta Mater. 52 (2004) 3889–3899.
[10] I. Mészáros, J. Prohászka, J. Mater. Proc. Tech. 161 (2005) 162–168.
[11] M. Botshekan, S. Degallaix, Y. Desplanques, Mater. Sci. Eng. A 234–236 (1997) 463–466.
[12] B.H. Sencer, S.A. Maloy, G.T. Gray, Acta Mater. 53 (2005) 3293–3303.
[13] I. Karaman, H. Sehitoglu, H.J. Maier, Y.I. Chumlyakov, Acta Mater. 49 (2001) 3919–3922.
[14] E.H. Lee, M.H. Yoo, T.S. Byun, J.D. Hunn, K. Farrell, L.K. Mansur, Acta Mater. 49 (16) (2001) 3277–3287.
[15] Z. Jiao, G.S. Was, J. Nucl. Mater. 382 (2008) 203–209.
[16] F.B. Pickering, Physical metallurgical development of stainless steels, in: Proceedings of the Conference on Stainless Steels 84, Gothenberg, Sweden, 1984, Institute of Metals, London, p. 2.
[17] Y. Katayama, M.I. Tsubota, Y. Saito, in: Proceedings of the Twelfth International Symposium on Environmental Degradation of Materials in Nuclear Power Systems – Water Reactors (2006). p. 31.
[18] R. Lin Peng, M. Odén, Y.D. Wang, S. Johansson, Mater. Sci. Eng. A 334 (2002) 215–222.
[19] J. Robertson, Corr. Sci. 32 (4) (1991) 443–465.
[20] J.P. Hirth, B. Pieraggi, R.A. Rapp, Acta Metall. Mater. 43 (3) (1995) 1065–1073.
[21] T. Magnin, R. Chieragatti, R. Oltra, Acta Metall Mater. 38 (7) (1990) 1313–1319.
[22] E.I. Meletis, K. Lian, W. Huang, Corrosion–deformation interactions, in: Proceedings CDI'92, Fontainebleau, France, 1992, Magnin T, Gras JM editors. Les Ulis: Les Editions de Physique, 1992, pp. 69–81.
[23] E. Andrieu, B. Pieraggi, A.F. Gourgues, Scripta Mater. 39 (4/5) (1998) 597–601.